High-order triangle-based discontinuous Galerkin methods for hyperbolic equations on a rotating sphere

Francis X. Giraldo *

Naval Research Laboratory, Marine Meteorology Division, 7 Grace Hopper Ave., Stop 2, Monterey, CA 93943-5502, USA

Abstract

High-order triangle-based discontinuous Galerkin (DG) methods for hyperbolic equations on a rotating sphere are presented. The DG method can be characterized as the fusion of finite elements with finite volumes. This DG formulation uses high-order Lagrange polynomials on the triangle using nodal sets up to 15th order. The finite element-type area integrals are evaluated using order $2N$ Gauss cubature rules. This leads to a full mass matrix which, unlike for continuous Galerkin (CG) methods such as the spectral element (SE) method presented in Giraldo and Warburton [A nodal triangle-based spectral element method for the shallow water equations on the sphere, J. Comput. Phys. 207 (2005) 129–150], is small, local and efficient to invert. Two types of finite volume-type flux integrals are studied: a set based on Gauss–Lobatto quadrature points (order $2N - 1$) and a set based on Gauss quadrature points (order $2N$). Furthermore, we explore conservation and advection forms as well as strong and weak forms. Seven test cases are used to compare the different methods including some with scale contractions and shock waves. All three strong forms performed extremely well with the strong conservation form with $2N$ integration being the most accurate of the four DG methods studied. The strong advection form with $2N$ integration performed extremely well even for flows with shock waves. The strong conservation form with $2N - 1$ integration yielded results almost as good as those with $2N$ while being less expensive. All the DG methods performed better than the SE method for almost all the test cases, especially for those with strong discontinuities. Finally, the DG methods required less computing time than the SE method due to the local nature of the mass matrix.
Published by Elsevier Inc.

1. Introduction

On spherical domains, the most natural solution strategy is to use spherical harmonics (spectral transform methods) on a Gaussian grid where the longitude and latitude are the spherical coordinates. However, choosing spherical harmonics eliminates any possibility of exploiting adaptive solution strategies. Furthermore, for

* Tel.: +1 831 656 4882; fax: +1 831 656 4769.
 E-mail address: giraldo@nrlmry.navy.mil.

solving relevant problems the numerical model must be run in a distributed-memory mode (such as with the message-passing interface). It is well known that the cost of spherical harmonics is $O(N_{lat}^3)$ where N_{lat} denotes the number of grid points in the latitudinal direction (south to north pole).

On the other hand, local methods (e.g., finite differences, elements, and volumes) cost on the order of $O(N_p^2)$, where N_p denotes the number of total grid points. If either adaptivity or unstructured grids are to be used then this now only leaves finite elements (FE) and finite volumes (FV) as the only two viable options. Typically, a choice has had to be made between high order accuracy and local conservation.

If high order accuracy (beyond 2nd order) is selected as the main criterion then the FE method must be the method selected. High order FE methods are typically referred to as spectral elements (SE) and we shall use these two terms interchangeably throughout this manuscript. FE/SE methods have shown to be quite capable of producing very accurate solutions for flows on rotating spheres (see [16]) provided that the solutions are smooth. However, if the solutions are non-smooth then FE/SE methods do not perform as well. We showed this in [13] in the context of unstructured quadrilateral elements and we show this in Section 5 for unstructured triangular elements.

However, if local conservation is the main criterion then FV methods must be chosen. FV methods have been shown to be quite effective in handling discontinuous flows on rotating spheres (see [24]). However, FV methods are at most second order accurate on unstructured triangular grids (see [10]); higher order reconstructions are only readily available for Cartesian (structured) grids and only using quadrilaterals.

Thus if both high order accuracy and local conservation on unstructured triangular grids are sought then the natural choice is the discontinuous Galerkin (DG) method. In essence, the DG method extracts the best features of FE and FV methods and fuses them into a powerful method capable of delivering high order accuracy in conjunction with local conservation. In [13], we introduced the first DG formulation for flows on a rotating sphere using much of the same machinery originally developed for SE methods (see [12]); the main difference being that we replaced the C^0 continuity condition of SE methods with a discontinuity at the element interfaces resolved via jump conditions in a similar vein to that of penalty methods (see [4]). Because the DG method shares much in common with FV methods then much of the same machinery developed for FV methods such as Riemann solvers, total variation diminishing (TVD) schemes, and nonlinear flux limiters can be applied to DG methods which then renders the solutions not only high-order accurate but also monotonicity preserving as well.

In addition to offering local conservation, high order accuracy, monotonicity, and adaptivity, the DG method also offers efficiency and natural *parallelization* especially for unstructured triangular grids. To clarify this point, in Fig. 1 we show the discrete stencil required by both the DG and SE methods. The DG stencil is
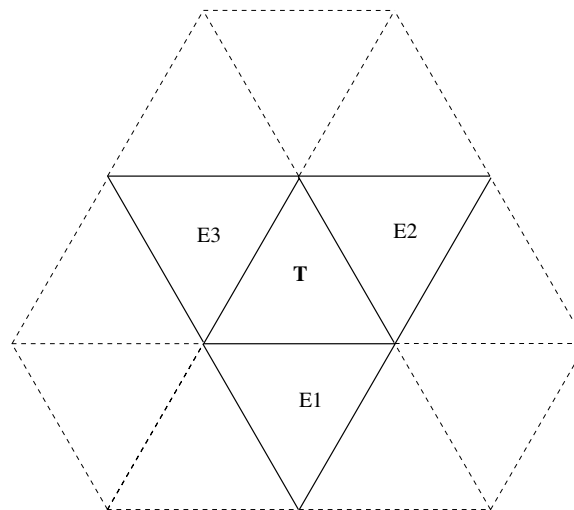

Fig. 1. The discrete stencil of the triangle, T, for the DG method (solid triangles) and the SE method (solid and dashed triangles).

shown by the solid triangles (4 triangles) and the SE stencil by both the solid and dashed triangles (13 triangles). Note that no matter how unstructured the grid becomes, the DG triangle will always have only 3 edge neighbors (E1, E2, and E3) to communicate with while the communication stencil of the SE triangle is much larger because the C^0 continuity condition is based on vertex neighbors. With grid adaptivity, the number of vertex neighbors for the SE triangle may change drastically from one grid generation to the next whereas the DG triangle will always have only three edge neighbors no matter how distorted the grid becomes.

It should be mentioned that recently robust high-order (3rd order) FV using weighted essentially non-oscillatory (WENO) reconstructions have been developed (see [8,18,26]) for unstructured triangular grids. There exists a 4th order reconstruction (see [18]) but it is not as geometrically flexible as its lower order cousins. WENO FV methods show great promise and higher order reconstructions are underway but the complexity in constructing the weighted differencing stencils may prove to be too daunting a task. Another recently developed conservative method that deserves mention is the spectral volume (SV) method [30]; however, the SV method is not a contender on spherical geometries because it requires planar straight-edged triangular elements whereas our applications require a method that can be constructed directly on curved spherical triangular elements. The advantage that the DG method has over WENO FV, SV, and all other methods is that it can be used on highly unstructured triangulations, on curved triangular elements, and to arbitrarily high order. Nonetheless, the DG method is not without its weakness; current research in DG methods focuses on the construction of robust TVD limiters for shock wave phenomena which we reserve for future work.

The remainder of the paper is organized as follows. Section 2 describes the governing equations of motion used to test our numerical method. In Section 3, we describe the discretization of the governing equations. This includes the spatial discretization by the triangle-based DG method and the time-integrator. In Section 4, we describe one of the many possible triangulations on a sphere. Finally, in Section 5 we present convergence rates for the four triangle-based DG methods and compare them with the SE method. This then leads to some conclusions about the performance of the various DG methods studied and a discussion on the direction of future work.

2. Continuous equations

The discontinuous Galerkin method we propose in this work is applicable to any nonlinear hyperbolic partial differential equation on a sphere. Thus at this point the only condition on the continuous equations is that the flow be inviscid – that is, the method is equally applicable to the Euler, Maxwell shallow water, and magneto-hydrodynamics shallow water equations. For the purposes of describing the algorithm we shall restrict our attention to the shallow water equations; in future work we shall address other equation sets.

The shallow water equations are a system of first order nonlinear hyperbolic equations which govern the motion of an inviscid incompressible fluid in a shallow depth. The predominant feature of this type of fluid is that the characteristic length of the fluid is far greater than its depth which is analogous to the motion of air in the atmosphere and water in the oceans. For this reason these equations are typically used as a first step toward the construction of either NWP, climate, or ocean models.

The shallow water equations on a sphere in Cartesian conservation form are

$$\frac{\partial \boldsymbol{q}}{\partial t} + \boldsymbol{\nabla} \cdot \boldsymbol{F}(\boldsymbol{q}) = S(\boldsymbol{q}), \tag{1}$$

where $\boldsymbol{q} = (\phi, \phi \boldsymbol{u}^{\mathrm{T}})^{\mathrm{T}}$ are the conservation variables.

$$\boldsymbol{F}(\boldsymbol{q}) = \begin{pmatrix} \phi \boldsymbol{u} \\ \phi \boldsymbol{u} \otimes \boldsymbol{u} + \frac{1}{2} \phi^2 \mathscr{I}_3 \end{pmatrix} \tag{2}$$

is the flux tensor and

$$S(\boldsymbol{q}) = -\begin{pmatrix} 0 \\ f(\boldsymbol{x} \times \phi \boldsymbol{u}) + \phi \boldsymbol{\nabla} \phi^{\mathrm{s}} + \mu \boldsymbol{x} \end{pmatrix} \tag{3}$$

is the source function where the nabla operator is defined as $\boldsymbol{\nabla} = (\partial_x, \partial_y, \partial_z)^{\mathrm{T}}$, $\otimes$ denotes the tensor product operator, ϕ is the geopotential height ($\phi = gh$ where g is the gravitational constant and h is the vertical height

of the fluid), ϕ^s is the surface topography (e.g., mountains), $\boldsymbol{u} = (u,v,w)^T$ is the Cartesian wind velocity vector, $f = \frac{2\omega z}{a^2}$ is the Coriolis parameter and (ω, a) represent the rotation of the earth and its radius, respectively. The term $\mathscr{I}_3$ is a rank-3 identity matrix, and the term $\mu\boldsymbol{x}$, where $\boldsymbol{x} = (x,y,z)^T$ is the position vector of the grid points, is a fictitious force introduced to constrain the fluid particles to remain on the surface of the sphere. Switching from spherical (2D) to Cartesian (3D) coordinates allows the fluid particles an additional degree of freedom; the Lagrange multiplier, μ, is introduced in order to prevent particles from flying off the sphere. The reason for using the Cartesian form of the equations is that the pole singularity associated with spherical coordinates is avoided and because this form, in conjunction with the mapping described in Section 3.1.1, allows for any curved surface to be discretized by this approach.

Alternatively, Eq. (1) can be recast in the advection form

$$\frac{\partial \boldsymbol{q}^A}{\partial t} + \boldsymbol{u}\cdot\nabla\boldsymbol{q}^A + \nabla\cdot\boldsymbol{P} = S(\boldsymbol{q}^A), \tag{4}$$

where $\boldsymbol{q}^A = (\phi, \boldsymbol{u}^T)^T$ is the solution vector.

$$\boldsymbol{P} = \begin{pmatrix} 0 & 0 & 0 \\ \phi & 0 & 0 \\ 0 & \phi & 0 \\ 0 & 0 & \phi \end{pmatrix} \tag{5}$$

is the pressure tensor, and

$$S(\boldsymbol{q}^A) = -\begin{pmatrix} \phi\nabla\cdot\boldsymbol{u} \\ f(\boldsymbol{x}\times\boldsymbol{u}) + \nabla\phi^s + \mu\boldsymbol{x} \end{pmatrix} \tag{6}$$

is the source function. The reason for considering the advection form of the equations is because we would like to be able to use semi-Lagrangian time-integrators (see [14]) in future work.

3. Discretization

In this section, we describe the discretization of the shallow water equations. In Section 3.1, we describe the spatial discretization by the discontinuous Galerkin method including: the choice of basis functions, integration, and construction of the semi-discrete problem using various DG formulations. In Section 3.2 we describe the explicit time-integrator.

3.1. Triangle-based discontinuous Galerkin method

3.1.1. Basis functions

To define the discrete local operators we begin by decomposing the spherical domain Ω into N_e conforming non-overlapping triangular elements Ω_e such that

$$\Omega = \bigcup_{e=1}^{N_e} \Omega_e.$$

It should be mentioned, however, that the condition on grid conformity is not required by the DG method; we only impose this condition for ease of exposition.

To perform differentiation and integration operations, we introduce the nonsingular mapping $\boldsymbol{x} = \Psi(\boldsymbol{\xi})$ which defines a transformation from the physical Cartesian coordinate system $\boldsymbol{x} = (x,y,z)^T$ to the local reference coordinate system $\boldsymbol{\xi} = (\xi,\eta,\zeta)^T$ such that (ξ,η) lies on the spherical surface tiled by the triangular elements defined by $\Omega_e = \{(\xi,\eta,\zeta), -1 \leqslant \xi, \eta \leqslant 1, \xi + \eta \leqslant 0, \zeta = 1\}$.

Let us now represent the local element-wise solution $\boldsymbol{q}$ by an Nth order polynomial in $\boldsymbol{\xi}$ as

$$\boldsymbol{q}_N(\boldsymbol{\xi}) = \sum_{i=1}^{M_N} L_i(\boldsymbol{\xi})\boldsymbol{q}_N(\boldsymbol{\xi}_i), \tag{7}$$

where ξ_i represents $M_N = \frac{1}{2}(N+1)(N+2)$ grid points and $L_i(\xi)$ are the associated multivariate Lagrange polynomials. For the grid points ξ_i we choose the nodal set derived from the electrostatics principle [17] for $N < 11$ and the Fekete points [28] for $11 \leqslant N \leqslant 15$. These sets were selected because they yield the lowest Lebesgue constants currently found in the literature. In [16] these nodal sets were shown to exhibit exponential convergence for the shallow water equations on the sphere using a spectral element formulation. The details on the construction of the Lagrange polynomial basis functions can be found in [16] where cardinal functions based on the Proriol–Koornwinder–Dubiner (PKD) polynomials [23,21,5] are used. Alternatively, one could also choose to use the PKD polynomials themselves as the basis functions as is done in [7,6] which then yields a modal representation (spectral or amplitude-frequency space) of the solution variables instead of the nodal representation (physical space) that we propose. Both the modal and nodal representations should yield the same accuracy; however, the difference between these two forms may be in their relative efficiencies (i.e., computational cost). In the future, comparison studies between these two forms should be performed in order to quantify their performance but for now we shall proceed only with the nodal representation.

3.1.2. Integration

Area integrals. In order to complete the discussion of the local element-wise operations required to construct discrete spatial operators we must describe the integration procedure required by the weak formulation of all Galerkin methods. For any two functions f and g the 2D (area) integration $\mathscr{I}_A$ proceeds as follows

$$\mathscr{I}_A[f,g] = \int_{\Omega_e} f(\boldsymbol{x})g(\boldsymbol{x})\,\mathrm{d}\boldsymbol{x} = \sum_{i=1}^{M_C} w_i |J(\xi_i)| f(\xi_i)g(\xi_i),$$

where M_C is a function of C which represents the order of the cubature approximation. For w_i and ξ_i we use the high-order cubature rules for the triangle given in [27,2,22,3]; because we use order $2N$ integration, which is exact for this equation set, then neither spatial filters nor smoothing diffusion operators are used in any of the DG simulations.

Boundary integrals. Unlike in continuous finite elements, such as the SE method, the DG method also requires the evaluation of boundary integrals which is the mechanism by which the fluxes across element edges are evaluated which then allows the discontinuous elements to communicate. For any two functions f and g the 1D (boundary) integration $\mathscr{I}_B$ proceeds as follows

$$\mathscr{I}_B[f,g] = \int_{\Gamma_e} f(\boldsymbol{x})g(\boldsymbol{x})\,\mathrm{d}\boldsymbol{x} = \sum_{i=0}^{Q} w_i |J(\xi_i)| f(\xi_i)g(\xi_i),$$

where Q represents the order of the quadrature approximation. Using Gauss quadrature we can use $Q = N$ to achieve order $2N$ accuracy. However, since the Fekete points are in fact Gauss–Lobatto points along the edges of the triangles then using $Q = N$ only achieves order $2N - 1$ accuracy but in this case integration amounts to sampling the functions f and g at the edge grid points only without the need to interpolate to a different quadrature grid; this then reduces the computation of fluxes from $\mathrm{O}(N_s N^2)$ to $\mathrm{O}(N_s N)$, where N_s is the total number of sides/edges in the grid.

3.1.3. Tangent and normal vectors of the element edges

Below it will become evident that in order to construct a discontinuous Galerkin discretization requires knowing a bit about the element geometry. In continuous Galerkin methods such as finite and spectral element methods the only required information is the basis functions, metric terms, and cubature rules. The DG method requires all of this finite element-type information plus some finite volume-type information regarding the element edges and the element neighbors sharing these edges. However, the good news for the DG method is that regardless of the order of the basis function, N, each element only has three edge neighbors. This is the process by which a DG element shares its local information with its neighbors. Fig. 2 shows a schematic of a master element along with its three normal vectors.
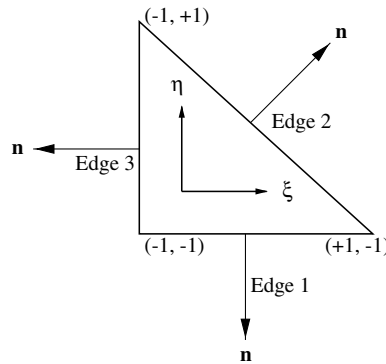
Fig. 2. The normal vectors of the master triangle.

Note that the tangent vectors for the three edges are given as follows:

- for edge 1 $t_1 = \frac{\partial x}{\partial \xi}$,
- for edge 2 $t_2 = -\frac{\partial x}{\partial \xi} + \frac{\partial x}{\partial \eta}$,
- for edge 3 $t_3 = -\frac{\partial x}{\partial \eta}$.

Now, let $r = \frac{x}{a}$ be the radial vector oriented from the origin (the center of the sphere) to the point x; on the master element given in Fig. 2 r points out of the paper. Then the normal vectors are computed as follows $n = t \times r$ which then must be normalized to unity. Although the radial vector, r, and the tangent vector, t, change along an edge its cross product, n, remains constant throughout; thus we only need to store one normal vector per edge regardless of the number of quadrature points along that edge.

3.1.4. Element node numbering

Clever strategies for storing the element edge data are required in order to compute tangent and normal vectors, grids, domain decomposition, and even graphics. For example, for quadrilateral-based SE or DG methods this is not an issue because tensor products of the 1D points are used to construct the 2D high-order stencil. Thus this assumes a natural order for the grid points. However, for triangle-based SE or DG methods the high-order points are quite random in the interior of the triangle (for Fekete points the edge points are in fact Gauss–Lobatto points). Thus one needs some way of ordering the points. Of course one could number the points randomly but this will then complicate many of the operations required by a specific computational model.

We propose the following numbering strategy: start from the point which corresponds to the local reference coordinate $\xi = -1$, $\eta = -1$ and call this the point 1. Then moving in a counterclockwise direction (see Fig. 2) along the points $-1 \leqslant \xi \leqslant 1$, $\eta = -1$ (edge 1) stores the first $N + 1$ points. Then moving from $N + 1$ to $2N + 1$ points we move along edge 2. Finally, from $2N + 1$ to $3N$ defines edge 3. Thus the first $3N$ points of the element connectivity matrix contains the perimeter values of the element stored in a CCW direction. The remaining $\frac{1}{2}(N - 1)(N - 2)$ points are the interior points and they are stored in no particular order. Recall that in the SE or DG method only the edge (perimeter) values are all that is needed in order to communicate with neighboring elements thus we only require the first $3N$ points of each element for these operations. In addition, for either computing grids or domain decomposition methods, this is the only data that is needed. For the purposes of graphics, that is plotting the data stored on high-order triangles, one does need some connectivity ordering of the interior grid points with the perimeter points. In fact, all of the contour plots shown in this manuscript are drawn by breaking down the high order points of each element into the internal triangulation of the so-called high-order cells. Then all one needs to do is to assume that each subcell is a linear element for the purposes of plotting the data and, as will be shown in Section 5, for computing Courant numbers.

3.1.5. Conservation form

Applying the discontinuous Galerkin discretization to the conservation form, Eq. (1), and using Green's theorem yields the classical DG form which we shall refer to as the *weak conservation* form

$$\int_{\Omega_e} \left(\frac{\partial \boldsymbol{q}_N}{\partial t} - \boldsymbol{F}_N \cdot \boldsymbol{\nabla} - S_N \right) L_i(\boldsymbol{x}) \, \mathrm{d}\boldsymbol{x} = - \int_{\Gamma_e} L_i(\boldsymbol{x}) \boldsymbol{n} \cdot \boldsymbol{F}_N^* \, \mathrm{d}\boldsymbol{x}, \tag{8}$$

where F_N is the polynomial representation of the function F given by Eq. (7). Note that Eq. (8) states that $\boldsymbol{q}_N$ satisfies the equation on each element Ω_e for all $L \in \mathscr{S}$ where $\mathscr{S}$ is the finite-dimensional space $\mathscr{S} = \{ L \in \mathscr{L}_2(\Omega) : L|_{\Omega_e} \in P_N(\Omega_e) \forall \Omega_e \}$ where P_N is the polynomial space defined on Ω_e and the union of these elements defines the entire global domain – that is, $\Omega = \bigcup_{e=1}^{N_e} \Omega_e$ with N_e representing the total number of triangular elements. $\boldsymbol{n}$ is the outward pointing normal vector of the element edge Γ_e and $\boldsymbol{F}_N^*$ is the Rusanov numerical flux

$$\boldsymbol{F}_N^* = \frac{1}{2} \left[\boldsymbol{F}_N(\boldsymbol{q}_N^{\mathrm{L}}) + \boldsymbol{F}_N(\boldsymbol{q}_N^{\mathrm{R}}) - |\lambda|(\boldsymbol{q}_N^{\mathrm{R}} - \boldsymbol{q}_N^{\mathrm{L}})\boldsymbol{n} \right], \tag{9}$$

where $\lambda = \max\left(|U^{\mathrm{L}}| + \sqrt{\phi^{\mathrm{L}}}, |U^{\mathrm{R}}| + \sqrt{\phi^{\mathrm{R}}} \right)$ with $U^{\mathrm{L,R}} = \boldsymbol{u}^{\mathrm{L,R}} \cdot \boldsymbol{n}$ being the normal component of velocity with respect to the edge Γ_e, and the superscripts L and R represent the left and right sides of the element edge. The normal vector $\boldsymbol{n}$ is defined as pointing outward from left to right. Numerous other numerical fluxes are possible (such as those based on either exact or approximate Riemann solvers) but we have chosen the Rusanov flux primarily due to its generality, simplicity, and efficiency (since the waves along an edge do not need to be mapped to the normal and tangential components typical of HLL and HLLC fluxes.). In future work, we shall explore different fluxes in connection with total variation diminishing (TVD) schemes; our results with Rusanov fluxes have shown similar results to those with HLL and HLLC fluxes while costing far less to compute.

Integrating Eq. (8) by parts once more yields the *strong conservation* form

$$\int_{\Omega_e} L_i(\boldsymbol{x}) \left(\frac{\partial \boldsymbol{q}_N}{\partial t} + \boldsymbol{\nabla} \cdot \boldsymbol{F}_N - S_N \right) \mathrm{d}\boldsymbol{x} = \int_{\Gamma_e} L_i(\boldsymbol{x}) \boldsymbol{n} \cdot \left(\boldsymbol{F}_N - \boldsymbol{F}_N^* \right) \mathrm{d}\boldsymbol{x}, \tag{10}$$

which although mathematically equivalent to the weak form, yields different numerical solutions.

Remark. The terms *strong* and *weak* forms refer to strong and weak Galerkin formulations. In other words in the strong form, it is evident what the continuous equations represent. This can be seen by comparing Eqs. (1) and (10). In contrast, the weak form uses integration by parts and thus the continuous and discrete equations look different; one can see this by comparing Eqs. (1) and (8).

Remark. In [13], we referred to the *strong*, Eq. (10), and *weak*, Eq. (8), conservation forms as the *divergence* and *Green*'s forms. In addition, we referred to the Rusanov flux, Eq. (9), as the Lax–Friedrichs flux. These two fluxes are equivalent if and only if the maximum wave speed, λ, approaches the Courant number which need not always be the case (e.g., see [29]).

3.1.6. Advection form

Applying the discontinuous Galerkin discretization to the advection form, Eq. (4), and using Green's theorem yields the *weak advection* form

$$\int_{\Omega_e} \left(\frac{\partial \boldsymbol{q}_N^A}{\partial t} - \boldsymbol{F}_N^A \cdot \boldsymbol{\nabla} - \boldsymbol{q}^A \boldsymbol{\nabla} \cdot \boldsymbol{u} - S_N^A \right) L_i(\boldsymbol{x}) \, \mathrm{d}\boldsymbol{x} = - \int_{\Gamma_e} L_i(\boldsymbol{x}) \boldsymbol{n} \cdot \boldsymbol{F}_N^{A,*} \, \mathrm{d}\boldsymbol{x}, \tag{11}$$

where

$$\boldsymbol{F}_N^A = \begin{pmatrix} \phi_N \boldsymbol{u}_N \\ \boldsymbol{u}_N \otimes \boldsymbol{u}_N + \phi_N \cdot \boldsymbol{\mathscr{I}}_3 \end{pmatrix} \tag{12}$$

is the flux tensor corresponding to the advection form of the equations.

Integrating Eq. (11) by parts once more yields the *strong advection* form

$$\int_{\Omega_e} L_i(\boldsymbol{x}) \left(\frac{\partial \boldsymbol{q}_N^A}{\partial t} + \boldsymbol{u}_N \cdot \boldsymbol{\nabla} \boldsymbol{q}_N^A + \boldsymbol{\nabla} \cdot \boldsymbol{P}_N - S_N^A \right) \mathrm{d}\boldsymbol{x} = \int_{\Gamma_e} L_i(\boldsymbol{x}) \boldsymbol{n} \cdot \left(\boldsymbol{F}_N^A - \boldsymbol{F}_N^{A,*} \right) \mathrm{d}\boldsymbol{x}. \tag{13}$$

Remark. The weak form of the DG, Eqs. (8) and (11), is easier to implement numerically because this form does not require constructing derivatives of the flux tensors, only the derivatives of the basis functions.

Remark. The strong form, Eqs. (10) and (13), is conceptually more attractive, and somewhat reminiscent of penalty methods, in that it amounts to satisfying the original equations in a local element sense with neighboring elements communicating only via the penalty/jump conditions represented by the flux terms on the right-hand-side of the equations. This is evident by comparing Eqs. (1), (10), and (4), (13).

Remark. Conventional wisdom discourages the use of the advection form for finite volume methods. The reason given is that this form is not guaranteed to converge to the correct solution when strong shocks are present. We study the DG in strong advection form to see if for the limited number of cases we study we see such behavior.

3.2. Time-integrator

In almost all DG formulations, the time-integrator is usually chosen to be some variant of Runge–Kutta (RK) methods. This family of time-integrators is selected because these methods are stable for eigenvalues off the imaginary axis. However, in many applications in geophysical fluid dynamics (GFD) semi-implicit methods based on second order leapfrog (LF2) have been the method of choice; however, LF2 does not work for DG precisely because the DG eigenvalues are more akin to parabolic equations rather than purely hyperbolic systems. Therefore in this work we propose backward difference formulas (BDF). For continuous Galerkin methods (such as finite and spectral element methods) the eigenvalues of the advection operator lie along the imaginary axis (see Fig. 3) and so LF2 is appropriate; however, for discontinuous Galerkin methods these eigenvalues now lie to the left of the imaginary axis precisely along the stability region of RK and BDF methods.

Since the DG method proposed in the present work is meant to appeal to researchers in both computational fluid dynamics (CFD) and GFD we shall use explicit backward difference formula (BDFK) originally proposed by Karniadakis et al. (see [20]).

For the set of ordinary differential equations

$$\frac{\partial \boldsymbol{q}}{\partial t} = \boldsymbol{S} \tag{14}$$

the Kth order BDF time-integrators with K-extrapolation (which we shall refer to as BDFK) yields:

$$\boldsymbol{q}^{n+1} = \sum_{m=0}^{K-1} \alpha_m \boldsymbol{q}^{n-m} + \gamma \Delta t \sum_{m=0}^{K-1} \beta_m \boldsymbol{S}^{n-m}, \tag{15}$$
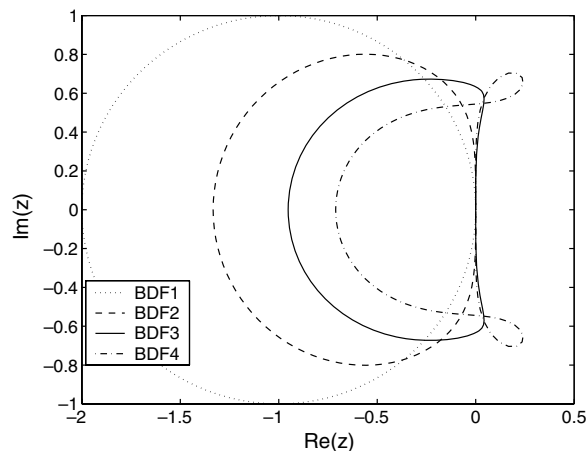

Fig. 3. The stability region of the BDFK methods.

Table 1
Coefficients of the backward difference formulas with extrapolation, BDFK, corresponding to Eq. (15)

	BDF1	BDF2	BDF3	BDF4	BDF5	BDF6
α_0	1	4/3	18/11	48/25	300/137	360/147
α_1	0	−1/3	−9/11	−36/25	−300/137	−450/147
α_2	0	0	2/11	16/25	200/137	400/147
α_3	0	0	0	−3/25	−75/137	−225/147
α_4	0	0	0	0	12/137	72/147
α_5	0	0	0	0	0	−10/147
γ	1	2/3	6/11	12/25	60/137	60/147
β_0	1	2	3	4	5	6
β_1	0	−1	−3	−6	−10	−15
β_2	0	0	1	4	10	20
β_3	0	0	0	−1	−5	−15
β_4	0	0	0	0	1	6
β_5	0	0	0	0	0	−1

which like RK methods, is stable for eigenvalues off the imaginary axis and is therefore as stable as RK but only requires one evaluation of the discrete operators per time-step. The αs correspond to the order of the time-derivative and the βs to the order of the extrapolation (see Table 1). Note that the coefficients of the BDFK are written in a slightly different manner from those presented in [25]; the reason for this has to do with our formulation which simplifies the construction of semi-implicit time-integrators (see [15]). In Table 1, we give the coefficients for the BDF1 to BDF6 and in Fig. 3 we show the stability regions of the BDF1 through BDF4; we omit BDF5 and BDF6 because their stability region is much smaller and thereby not worthy of further consideration but include them nonetheless for completeness.

In the test cases studied we have not seen much difference between the different BDFKs and so, for simplifying the comparison with previously used second order time-integrators we use exclusively BDF2; in addition, the BDF2 method that we used has been shown to be total variation diminishing (TVD) by Hundsdorfer and Jeffré [19] (for a stability analysis of DG with BDF2 see this reference). We have used this BDF2 method quite successfully for semi-implicit hydrostatic primitive equation models [15] and semi-Lagrangian shallow water models [14], both using SE discretizations. It turns out that BDF2 and RK2 have similar stability regions; however, the fact that BDF2 only requires one evaluation of the discrete operators per time step means that it is more efficient than RK2; we have not done the same comparisons for $K \geqslant 3$ but we suspect that the RK methods may prevail in terms of efficiency at these larger K values. Regardless, in [15] we showed that BDF2 is a good choice also for SE discretization of hyperbolic equations because no temporal filter is required. Thus the DG methods we present here in conjunction with the BDF2 time-integrator do not require neither spatial nor temporal filters of any kind; in fact none are used in this paper.

4. Triangulation on a sphere

The choice of which triangulation to use for the sphere is not obvious. Commonly, grids are chosen which simplify the construction of the discrete operators. For example, latitude–longitude grids are used with spectral transform methods because these are the only grids that can be used with this method. The hexahedral grid (i.e., the cubed-sphere) has been used with finite difference, finite volume, and spectral element methods because each of the six faces of the cube map onto a logically Cartesian geometry that allows for the simple and rapid construction of the discrete operators. Picking one grid and constructing the discrete operators on a specific grid geometry simplifies matters but it also dictates the algorithm thereby losing any hope of using other types of grids and adaptive solution strategies.

In our case, the DG method is constructed in a very general way such that the model reads in any grid geometry and then constructs the discrete operators directly on the grid. This allows the use of any grid and offers the freedom to choose the best possible grid for specific applications. For the purposes of validating the triangle-based DG methods we shall use a disjointed set of triangles formed by the subdivision of the triangular faces of an icosahedron; however, it should be understood that any triangular grid can be used; other possible triangulations are presented in [16] and in fact we use an adaptive unstructured grid to prove this point.
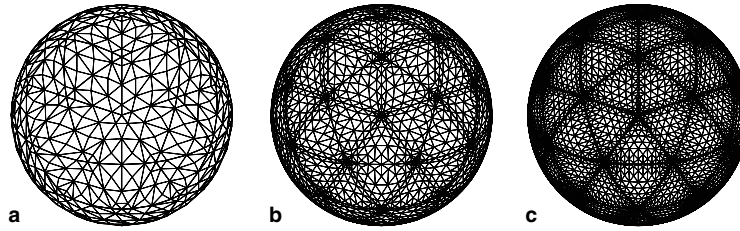
Fig. 4. Icosahedral grid for $n_I = 2$ and (a) $N = 4$, (b) $N = 8$, and (c) $N = 12$.

To construct icosahedral grids we consider the initial icosahedron and subdivide each of the initial triangles by a Lagrange polynomial of order n_I. Prior to mapping these elements onto the sphere it is convenient to map the triangles onto a gnomonic space. The most unbiased mapping is obtained by mapping about the centroid of the triangles.

Let (λ_c, θ_c) be the centroid of the triangle we wish to map where λ represents the zonal (east-west) and θ the meridional (north–south) directions. The gnomonic mapping is then given by

$$
\begin{aligned}
X &= \frac{a \cos \theta \sin(\lambda - \lambda_c)}{\sin \theta_c \sin \theta + \cos \theta_c \cos \theta \cos(\lambda - \lambda_c)}, \\
Y &= \frac{a[\cos \theta_c \sin \theta - \sin \theta_c \cos \theta \cos(\lambda - \lambda_c)]}{\sin \theta_c \sin \theta + \cos \theta_c \cos \theta \cos(\lambda - \lambda_c)},
\end{aligned}
\tag{16}
$$

where $X \in [-1, +1]^2$ in the equi-distant gnomonic space G. To simplify matters, we first apply a rotation whereby Eq. (16) becomes

$$X = a \tan \lambda_R, \quad Y = a \tan \theta_R \sec \lambda_R,$$

in the new coordinate system with the centroid (λ_c, θ_c) located at $(0,0)$. The rotation mapping is given as

$$
\begin{aligned}
\lambda_R &= \arctan \left[\frac{\cos \theta \sin(\lambda - \lambda_c)}{\sin \theta_c \sin \theta + \cos \theta_c \cos \theta \cos(\lambda - \lambda_c)} \right], \\
\theta_R &= \arcsin \left[\cos \theta_c \sin \theta - \sin \theta_c \cos \theta \cos(\lambda - \lambda_c) \right].
\end{aligned}
$$

This approach enables the construction of an icosahedral grid with the following properties

$$N_{\mathrm{p}} = 10(n_I N)^2 + 2, \tag{17}$$

$$N_{\mathrm{e}} = 20(n_I)^2, \tag{18}$$

$$N_{\mathrm{s}} = 30(n_I)^2, \tag{19}$$

where N_{p}, N_{e}, and N_{s} denote the number of points, elements, and sides/edges comprising the triangular grid, and n_I controls the number of triangular elements while N denotes the order of the polynomial inside each element. Fig. 4 provide examples of grids for $n_I = 2$ and $N = 4$, 8 and 12. All the grids illustrated are viewed from the North Pole where the thick lines denote the elements and the thin lines are the high-order grid points. It should be understood that the grids we use here are not polyhedra (i.e., the triangular elements are not flat planes) but rather are exact curved representations of the sphere. Therefore, the basis functions defined in Section 3.1.1 are constructed directly on the spherical geometry such that all the Fekete points within each element lie on the sphere. This implies that the triangles are in fact spherical triangles which is important in order to achieve spectral convergence.

5. Numerical experiments

For the numerical experiments, we use the normalized L_2 error norm

$$\|\boldsymbol{\phi}\|_{L_2} = \sqrt{\frac{\int_\Omega (\boldsymbol{\phi}_{\mathrm{exact}} - \boldsymbol{\phi})^2 \, \mathrm{d}\Omega}{\int_\Omega \boldsymbol{\phi}_{\mathrm{exact}}^2 \, \mathrm{d}\Omega}}$$

to judge the accuracy of the SE methods. To compute the Courant number the elements are decomposed into their high-order (HO) grid points and these grid points form a fine grid which we refer to as the HO cells. The velocities and grid spacings are then defined at the centers of these cells. Using these definitions the Courant number is then defined as

$$\text{Courant number} = \max\left(\frac{C\Delta t}{\Delta s}\right)^e_{\text{HO}} \quad \forall e \in [1, \ldots, N_e],$$

where

$$C = \begin{cases} U & \text{for cases 1 and 4,} \\ U + \sqrt{\phi} & \text{for cases 2, 3, 5, 6, and 7,} \end{cases}$$

where C is the characteristic speed, $U = \sqrt{\boldsymbol{u} \cdot \boldsymbol{u}}$, and $\Delta s = \sqrt{\Delta x^2 + \Delta y^2 + \Delta z^2}$ is the grid spacing. For all the results presented the Courant number is taken to be $\leqslant 0.2$ which is the region of stability for BDF2 (see [15]).

Seven test cases are used to judge the performance of the triangle-based DG methods. Cases 1–3 correspond to the Williamson et al. standard test case suite [31] and represent solutions which are free of shocks or steep gradients. Cases 4–7 are good for testing the ability of a numerical method to handle discontinuities.

5.1. Test cases

For all of the test cases we compare four versions of the high-order triangle-based DG method: the strong conservation form with O(2N) integration, the weak conservation form with O(2N) integration, the strong advection form with O(2N) integration, and the strong conservation form with O(2N − 1) integration. The difference between the O(2N) and O(2N − 1) forms is that in the former Gauss integration points are used to evaluate the flux integrals whereas in the latter Gauss–Lobatto (GL) integration points are used. Thus since the interpolation points of the triangle along an edge are in fact GL points this means that the interpolation and integration points are co-located. This allows for a very efficient evaluation of flux integrals. However, one of the questions we would like to answer is how large a loss in accuracy will be incurred by using this performance enhancing strategy. In addition, we compare the DG methods with the recently developed nodal triangle-based spectral element (SE) method with O(2N) integration given in Giraldo and Warburton [16]. We begin with three test cases with relatively simple flow.

5.1.1. Case 1: passive advection of a cosine wave
Case 1 concerns the solid body rotation of a cosine wave. The velocity field remains unchanged throughout the computation. Williamson et al. [31] recommend that the error be computed after 12 days of integration which corresponds to one complete revolution of the cosine wave.

Fig. 5 shows the results of case 1 as a function of polynomial order, N, for the icosahedral grid refinement level $n_I = 2$. The results for this test show that there is almost no difference between the four DG methods. Furthermore, the DG methods compare quite well with the SE method; the SE method gives slightly more accurate solutions near $N = 6$ but otherwise all the methods yield similar results. Note that the initial condition for this case is not infinitely differentiable and so for this reason one cannot achieve exponential convergence.

5.1.2. Case 2: steady-state nonlinear zonal geostrophic flow
This case is a steady-state solution to the nonlinear shallow water equations. The equations are geostrophically balanced and remain so for the duration of the integration where the velocity field remains constant throughout the computation. The geopotential height ϕ undergoes a solid body rotation but since the initial height field is given as a constant band in the zonal direction and the flow field is purely zonal, then the solution remains unchanged throughout the time-integration. The velocity field is the same as that used in case 1. Williamson et al. [31] recommend that the error be computed after 5 days.

Fig. 6 shows the results of case 2 as a function of polynomial order, N, for the icosahedral grid refinement level $n_I = 2$. For this test the strong conservation forms perform better than the weak and advection forms and the SE method. Note that the strong conservation form does quite well even when order O(2N − 1) integration
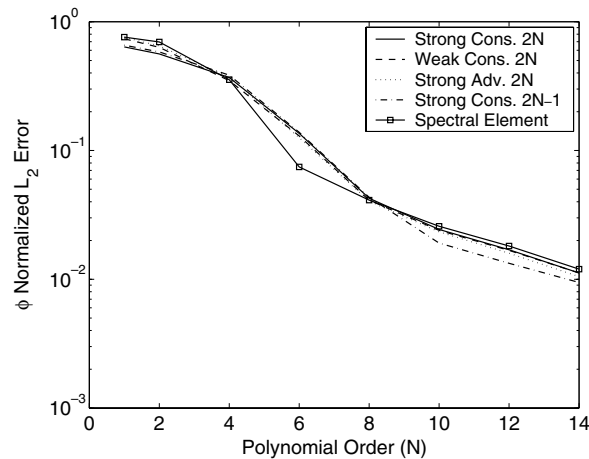
Fig. 5. Case 1. The normalized ϕL_2 error as a function of polynomial order, N, after 12 days using 80 ($n_I = 2$) elements for the strong conservation form with O($2N$) integration (solid line), weak conservation form with O($2N$) integration (dashed line), strong advection form with O($2N$) integration (dotted line), strong conservation form with O($2N - 1$) integration (dashed-dotted line), and the spectral element method (solid line with square).
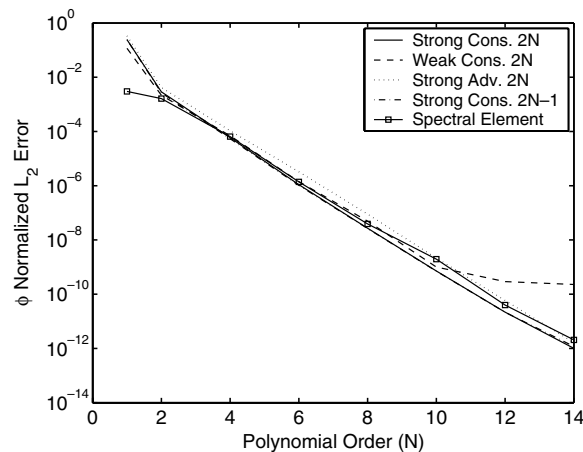

Fig. 6. Case 2. The normalized ϕL_2 error as a function of polynomial order, N, after 5 days using 80 ($n_I = 2$) elements for the strong conservation form with O($2N$) integration (solid line), weak conservation form with O($2N$) integration (dashed line), strong advection form with O($2N$) integration (dotted line), strong conservation form with O($2N - 1$) integration (dashed-dotted line), and the spectral element method (solid line with square).

is used. The weak form clearly yields the worst solution. In fact, the weak form is the only one that does not exhibit exponential convergence.

5.1.3. Case 3: steady-state nonlinear zonal geostrophic flow with compact support

This case is another steady-state solution to the nonlinear shallow water equations where the equations remain geostrophically balanced for the duration of the integration. The initial velocity field is zero everywhere except in a very small isolated region. This isolated region, or jet, encapsulates the flow and confines the geopotential height field to remain within a localized circular region. The results are reported for a 5-day integration as suggested in [31].

Fig. 7 shows the results of case 3 as a function of polynomial order, N, for the icosahedral grid refinement level $n_I = 2$. For this test all the DG methods yield the same exponentially convergent solution. In addition, all DG methods yield better solutions than the SE method for $N \geqslant 6$.
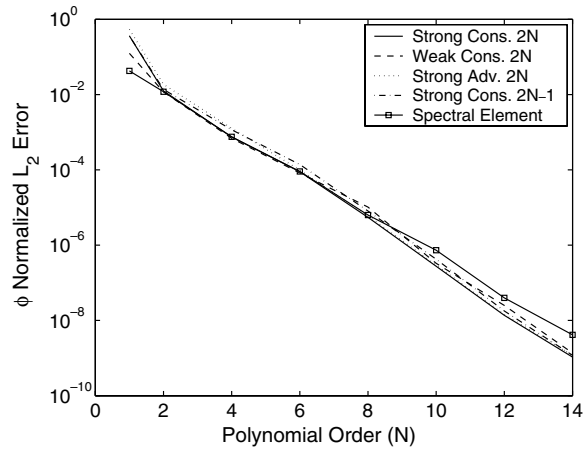
Fig. 7. Case 3. The normalized ϕL_2 error as a function of polynomial order, N, after 5 days using 80 ($n_I = 2$) elements for the strong conservation form with O($2N$) integration (solid line), weak conservation form with O($2N$) integration (dashed line), strong advection form with O($2N$) integration (dotted line), strong conservation form with O($2N - 1$) integration (dashed-dotted line), and the spectral element method (solid line with square).

5.1.4. Case 4: passive advection of a cylinder

This test case is similar to case 1 except that the cosine wave is replaced by a cylinder which is essentially the 2D analog of the 1D square pulse problem. This case is run for 12 days at which point the waves travel across the entire sphere.

Fig. 8 shows the results of case 4 as a function of grid refinement level, n_I, for order $N = 1$ elements. We have chosen the lowest polynomial order because since we are not using TVD spatial discretization methods in the current scheme then higher order polynomials will contribute virtually nothing to the accuracy of this non-smooth test (i.e., will not yield exponential convergence). For this test we can see that all four DG methods yield virtually similar results except for the DG with order O($2N - 1$) integration. This test case contains a scale contraction and for such problems it is very important to compute the flux integrals as accurately as possible. The similarities between the strong conservation and advection forms are not surprising because for a scalar conservation law these two forms are identical. All four DG methods perform better than the SE
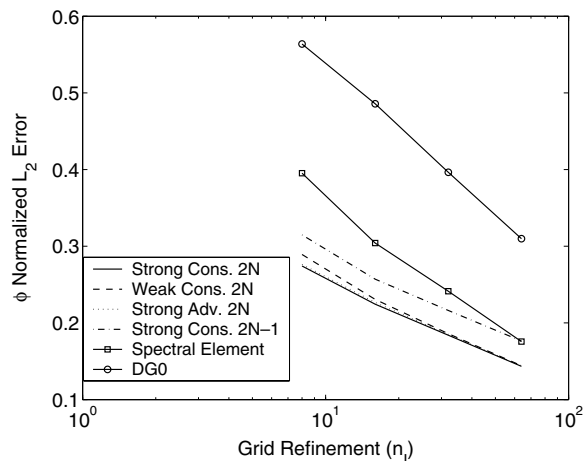

Fig. 8. Case 4. The normalized ϕL_2 error as a function of grid refinement, n_I, after 12 days using $N = 1$ order elements for the strong conservation form with O($2N$) integration (solid line), weak conservation form with O($2N$) integration (dashed line), strong advection form with O($2N$) integration (dotted line), strong conservation form with O($2N - 1$) integration (dashed-dotted line), spectral element method (solid line with square), and the DG0 method (solid line with circle).

method; however, the SE method catches up to the DG with $O(2N-1)$ integration at $n_I = 9$. We have also included a zeroeth order DG scheme (DG0) which is obtained by using the $N = 1$ DG solution and then extracting all of the modes except the $N = 0$ in order to make it equivalent to a cell-centered finite volume method. Unlike the remainder of the methods shown in Fig. 8, the DG0 method is first order accurate and it clearly does not do as well as the rest of the methods.

However, showing error norms does not tell the entire story. To show the difference in the solutions between the DG and SE methods we plot the geopotential height profile along the Equator in Fig. 9 for the resolution $n_I = 64$. The DG strong conservation form with $O(2N)$ integration (Fig. 9(a)) yields a relatively smooth solution with only minimal, and more importantly, localized undershoots and overshoots; in contrast, the SE solution (Fig. 9(b)) experiences spurious oscillations throughout the entire domain (global influence). This difference in behavior is due to the highly localized differencing stencil of the DG method which is a direct consequence of allowing the solution across element interfaces to be discontinuous. On the other hand, the SE method requires C^0 continuity across element interfaces which then allows Gibbs phenomena to pollute the entire domain during long time-integrations.

While the error norms shown in Fig. 8 for the DG0 method do not appear to be sufficiently accurate, Fig. 9(c) shows that the solution does not experience unphysical extrema. Again, because this solution is first order it will be monotone and this property has very important implications. We are not suggesting that the DG0 method should be used in the present form, rather, we suggest that the monotonicity of the DG0 method should be exploited in order to construct TVD or flux-corrected transport (FCT) DG schemes by carefully blending the low order monotone solution obtained with DG0 and the high order DG solution of order N; however, this is beyond the scope of the current work and we shall reserve it for future work. The point here is that even with a nodal basis, the DG method can be made to be TVD.

5.1.5. Case 5: cylindrical shock wave on a stationary sphere

This test case is a Riemann problem for the full nonlinear shallow water equations. A cylinder of fluid ($h = 100$ m) with radius $R = \frac{a}{3}$ is placed at $(\lambda, \theta) = (180, 0)$, where λ is longitude and θ is latitude, with zero velocity field and no Coriolis ($f = 0$). The shock wave collapses onto itself and begins to propagate through the sphere. This case is run for 5.4 days at which point the waves travel to the other side of the sphere where they collide culminating in a strong discontinuity centered at $(\lambda, \theta) = (0, 0)$. Slight variations of this test have been used recently for shallow water flows by Ata and Soulaimani [1] on the plane, and Rossmanith et al. [24] on the sphere.

The next few figures show results at various times in the integration for the grid resolution $n_I = 64$ and $N = 1$. This test illustrates the reasons for considering DG methods over standard finite/spectral element methods. In Fig. 10, we show the results as profiles of the geopotential height along the Equator as a function of longitude.

Fig. 10 shows the results after a half day. The cylinder initially centered at $\lambda = 180$ collapses onto itself forming a spike. The DG conservation forms yield identical solutions (Fig. 10(a)). The behavior of the advection form upstream of the shocks (Fig. 10(b)) is very surprising; note that there are very minimal undershoots
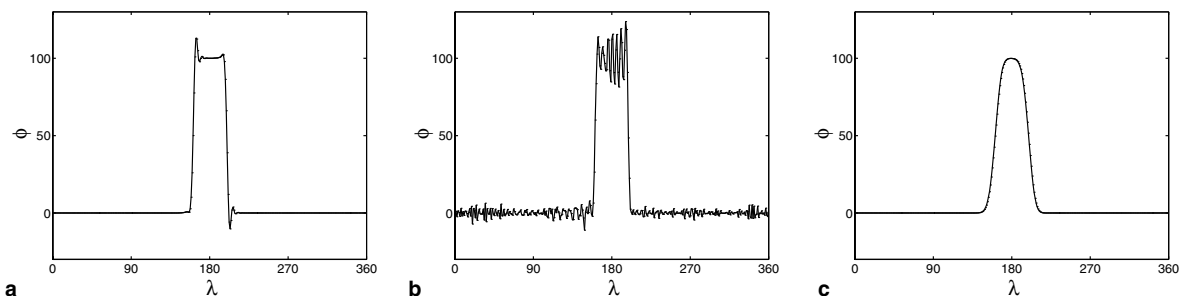

Fig. 9. Case 4. Profile of the geopotential height, ϕ, along the Equator after 12 days for $n_I = 64$ and $N = 1$ for the (a) DG strong conservation form with $O(2N)$ integration, (b) spectral element, and (c) the DG0 method.
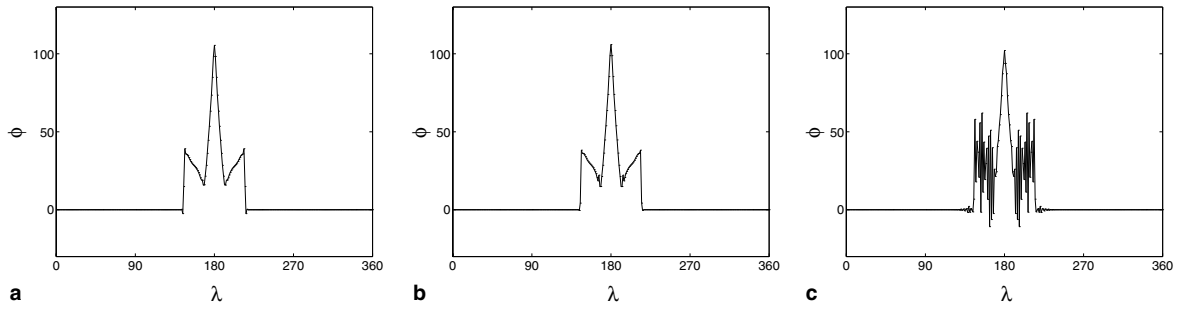
Fig. 10. Case 5. Profile of the geopotential height, ϕ, along the Equator after 0.5 days for $n_I = 64$ and $N = 1$ for the (a) conservation forms, (b) strong advection form, and (c) spectral element method.

in these regions as compared to the conservation forms. The spectral element (Fig. 10(c)) even with a strong filter (Boyd–Vandeven filter at 20% strength applied every 10 time-steps, see [16]) cannot handle the shocks very well; the undershoots and overshoots severely pollute the solution. This is a good example of the spurious oscillations (Gibbs phenomena) typically exhibited by non-monotone schemes in the presence of strong discontinuities.

Snapshots of the geopotential are illustrated in Fig. 11 for various times in the integration. Fig. 11(a)–(c) are shown from the viewpoint $(\lambda, \theta) = (180, 0)$ and Fig. 11(d)–(f) from $(\lambda, \theta) = (0, 0)$. Fig. 11(a)–(c) show the cylindrical shock wave expanding and propagating towards the other hemisphere. Fig. 11(d)–(f) show the wave culminating into a point singularity at which point the shock wave collapses onto itself and the shock evolution begins anew. However, beyond this point in the integration it is very difficult to discern whether the shock evolution dynamics is correct. The reason being that too many nonlinear interactions (such as colliding shocks) occur; however, the DG model has no difficulties with these dynamics and animations of 12 day integrations can be found at www.nrlmry.navy.mil/~giraldo/projects/dg_tri/dg_tri_movies.html. It is very difficult to fully appreciate these shock dynamics without viewing the animations.

The snapshots of the solution for case 5 at various times are shown for three reasons. First, the solutions show that the grid along with the DG method retains perfect symmetry with respect to longitude and latitude throughout the integration. Second, we have tried to mimic an animation by showing the dynamics at different
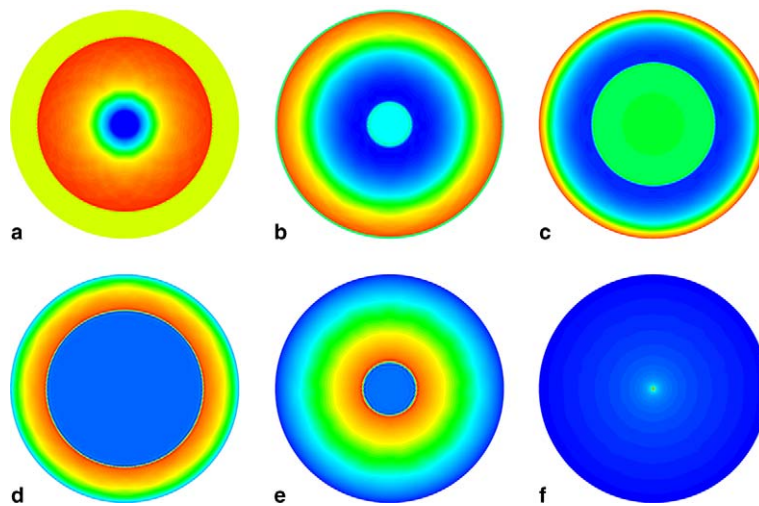

Fig. 11. Case 5. Color contours of ϕ (left), u_s (center), and v_s (right) for the DG strong conservation form with O(2N) integration for the resolution $n_I = 64$ and $N = 1$ at (a) 1 day, (b) 2 days, (c) 3 days, (d) 4 days, (e) 5 days, and (f) 5.4 days. (a–c) are viewed from $(\lambda, \theta) = (180, 0)$ and (d–f) from $(\lambda, \theta) = (0, 0)$.

points in the integration. Third, these snapshots give a reference to which to contrast case 6 which is similar in every respect to this case except that the sphere rotates (Coriolis effects are included).

5.1.6. Case 6: cylindrical shock wave on a rotating sphere

This case is similar to case 6 except that we now introduce Coriolis. The rotation of the sphere vastly changes the time-evolution of the shocks. Unfortunately, this case does not have a known analytic solution.

Snapshots of the geopotential are illustrated in Fig. 12 for the strong conservation form with O(2N) integration. For this plot all of the views are from $(\lambda, \theta) = (180, 0)$ since much of the more interesting dynamics occurs in this hemisphere. Fig. 12 clearly shows a different shock evolution from case 5 as the addition of Coriolis vastly changes how the shock propagates. While it is very difficult to see from only viewing these snapshots, the initial cylindrical shock collapses onto itself triggering radially propagating waves which, in the absence of Coriolis would evolve as in case 5. However, the rotating sphere causes the radially outward propagating waves to fold inward which can be clearly seen in Fig. 12(a). This inward folding motion causes the shock to shear into two components (Fig. 12(b)) which propagate in opposite directions; the left moving waves are Rossby waves and the right moving waves are Kelvin waves. Fig. 12(c)–(f) show the continued shearing of these waves which results in the long filaments visible in Fig. 12(f). While the exactness of these dynamics cannot be confirmed the waves visible in Fig. 12 are certainly predicted by linear theory. Animations of this test case can also be found at the previously mentioned link.

This type of simulation represents a very challenging test case for all numerical methods especially those that are being proposed for very fine-scale flows. Although the SE method we presented in [16] is exponentially convergent for smooth flows it is not so good for flows containing shocks. This is true of almost all existing methods except those that employ some form of Godunov-type method such as a Riemann solver; however, the SE method can be quite easily recast into a DG formulation such as the ones we have presented here. It should be emphasized that much better solutions (having absolutely no undershoots and overshoots) are possible with the DG method in combination with TVD flux-limiters which we reserve for future work. It is anticipated that the MUSCL-TVD methods we developed in [10,11] for finite volume methods on unstructured triangular grids can be extended to DG formulations.

5.1.7. Case 7: cylindrical shock wave on a stationary sphere with adaptivity

We now rerun the Riemann problem (case 5) except that now we use fixed adaptive grids. That is, we construct a grid at the initial time which is aligned with the flow and allow the shock waves to form and propagate on this fixed grid.
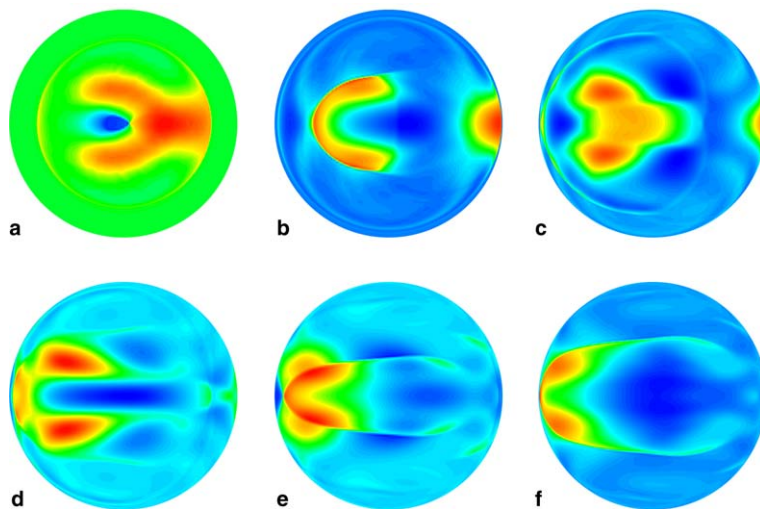

Fig. 12. Case 6. Color contours of ϕ (left), u_s (center), and v_s (right) for the DG strong conservation form with O(2N) integration for the resolution $n_1 = 64$ and $N = 1$ at (a) 1 day, (b) 2 days, (c) 3 days, (d) 4 days, (e) 5 days, and (f) 5.4 days. All the figures are viewed from $(\lambda, \theta) = (180, 0)$.
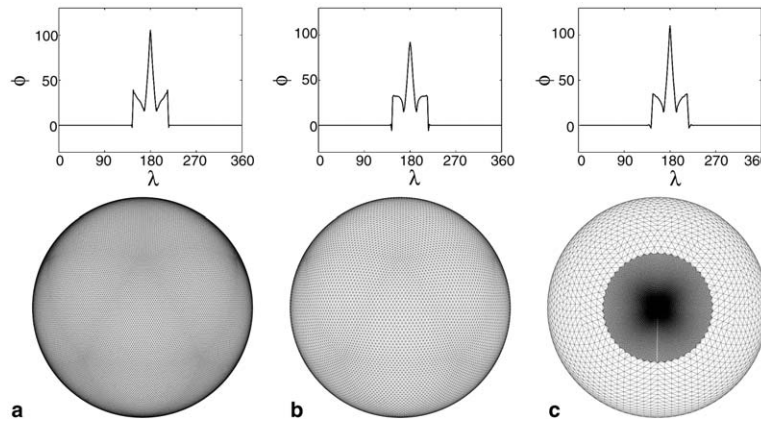
Fig. 13. Case 7. Profile of the geopotential height, ϕ, along the Equator and corresponding grid after 0.5 days for the DG strong conservation with O($2N$) integration on (a) icosahedral grid with 40,962 grid points ($n_I = 64$), (b) icosahedral grid with 16,002 grid points ($n_I = 40$), and (c) adaptive grid with 15,695 grid points.

Fig. 13 shows the results after a half day on icosahedral grids (left and center panels) and an adaptive grid (right panel). Note that the adaptive grid (Fig. 13(c)) has half as many grid points as the high-resolution icosahedral grid (Fig. 13(a)) and about the same number of grid points as the other icosahedral grid (Fig. 13(b)). Even though the adaptive grid uses almost half as many grid points as the high resolution grid it represents the shock just as well; note how the shock capturing capabilities of the method degrade with the coarser resolution (Fig. 13(b)) which is especially evident near the base of the shock where the shock is no longer as crisp. The success of the adaptive grid should not be surprising since a fine grid is used in the region where the shock lies and a coarse grid away from the shock; nonetheless, we use this case merely to show how simple it is to construct adaptive solutions using triangle-based DG methods. The interested reader is referred to [16] for details on the triangulation procedure used to generate the adaptive grids.

5.2. Computational cost

To compare the performance of the four DG methods and the SE method in Fig. 14 we report wallclock times for case 5 for a one day integration on a Dell PC with an Intel Xeon 1.8 Gigahertz processor. Not
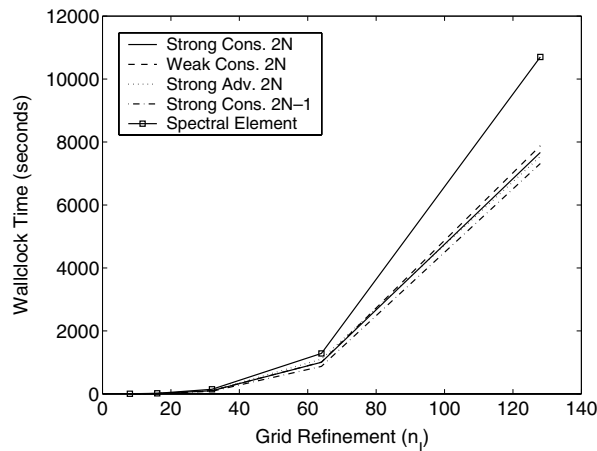

Fig. 14. The wallclock time required to perform a one day integration as a function of grid refinement level, n_I, using $N = 1$ for the strong conservation form with O($2N$) integration (solid line), weak conservation form with O($2N$) integration (dashed line), strong advection form with O($2N$) integration (dotted line), strong conservation form with O($2N - 1$) integration (dashed-dotted line), and the spectral element method (solid line with square).

surprisingly all of the DG methods give very similar performance with the strong conservation form with $O(2N-1)$ integration being the fastest. Note how much more costly the SE method is even with the aid of a state-of-the-art iterative solver (GMRES with a fast projection method, see [16]).

As the grid resolution is increased this gap in performance between the triangle-based SE and DG methods will continue to increase in favor of the DG methods. Recall that for spectral elements on triangles the mass matrix is not diagonal. Thus even when explicit time-integrators are used the SE method requires the inversion of a sparse global mass matrix (see [16]). For the triangle-based DG method (using cardinal functions based on the PKD polynomials) a mass matrix must still be inverted but it is local and quite small which allows for very efficient explicit time-integration. We are exploring semi-implicit time-integrators for both the triangle-based SE and DG methods.

6. Conclusions

Triangle-based discontinuous Galerkin methods for flows on a rotating sphere were presented. Strong and weak conservation forms as well as the strong advection form were studied. For the test cases studied, the strong conservation form with $O(2N)$ integration was the most robust. In general, all of the strong forms performed quite well. The weak conservation form gave similar results to the strong conservation for all cases except for one (case 2). The strong conservation form with $O(2N-1)$ integration performed extremely well for the cases with smooth flow (cases 1, 2, and 3); however, for the case with the scale contraction (case 4) it did not do as well. Surprisingly though, for the case with the shock wave (case 5) this form performed rather well. The DG forms with $O(2N)$ integration performed well for all the test cases.

For the test cases with smooth flow all of the DG forms gave similar or better results than the SE method with one exception (the weak conservation form in case 2). However, for the cases with non-smooth flows all of the DG forms gave far better results than the SE method. In addition, all of the triangle-based DG forms are more efficient than the triangle-based SE method. The reason being that for the triangle-based SE method a large global mass matrix must be inverted at every time step whereas in the DG method this mass matrix is small, local, and easy to invert.

The good results obtained with the triangle-based DG method for smooth and non-smooth flows on a rotating sphere are very exciting and in future work we plan to apply this method to other equation sets. In the current work, we only show one result with adaptive grids but in future work we plan to use adaptive grids in conjunction with more sophisticated Riemann solvers and total variation diminishing schemes for a detailed study of shock wave phenomena on rotating and non-rotating spheres.

Acknowledgements

References

[1] R. Ata, A. Soulaimani, A stabilized SPH method for inviscid shallow water flows, International Journal for Numerical Methods in Fluids 47 (2005) 139–159.

[2] R. Cools, P. Rabinowitz, Monomial cubature rules since Stroud: a compilation, Journal of Computational and Applied Mathematics 48 (1993) 309–326.

[3] R. Cools, Monomial cubature rules since Stroud: a compilation – Part 2, Journal of Computational and Applied Mathematics 112 (1999) 21–27.

[4] P.J. Diamessis, J.A. Domaradzki, J.S. Hesthaven, A spectral multidomain penalty method model for the simulation of high Reynolds number localized incompressible stratified turbulence, Journal of Computational Physics 202 (2005) 298–322.

[5] M. Dubiner, Spectral methods on triangles and other domains, Journal of Scientific Computing 6 (1991) 345–390.

[6] F. Dupont, C.A. Lin, The adaptive spectral element method and comparisons with more traditional formulations for ocean modeling, Journal of Atmospheric and Oceanic Technology 21 (2004) 135–147.

[7] C. Eskilsson, S.J. Sherwin, A triangular spectral/hp discontinuous Galerkin method for modelling 2D shallow water equations, International Journal for Numerical Methods in Fluids 45 (2004) 605–623.

[8] O. Friedrich, Weighted essentially non-oscillatory schemes for the interpolation of mean values on unstructured grids, Journal of Computational Physics 144 (1998) 194–212.

[10] F.X. Giraldo, A space marching adaptive remeshing technique applied to the 3D Euler equations for supersonic flow, PhD thesis, University of Virginia, 1995.

[11] F.X. Giraldo, A finite volume high resolution 2D Euler solver with adaptive grid generation on high performance computers, in: M. Morandi-Cecchi, K. Morgan, J. Periaux, B.A. Schrefler, O.C. Zienkiewicz (Eds.), Proceedings of the 9th International Conference on Finite Element in Fluids, Venice, Italy, 1995.

[12] F.X. Giraldo, A spectral element shallow water model on spherical geodesic grids, International Journal for Numerical Methods in Fluids 35 (2001) 869–901.

[13] F.X. Giraldo, J.S. Hesthaven, T. Warburton, Nodal high-order discontinuous Galerkin methods for the spherical shallow water equations, Journal of Computational Physics 181 (2002) 499–525.

[14] F.X. Giraldo, J.B. Perot, P.F. Fischer, A spectral element semi-Lagrangian (SESL) method for the spherical shallow water equations, Journal of Computational Physics 190 (2003) 623–650.

[15] F.X. Giraldo, Semi-implicit time-integrators for a scalable spectral element atmospheric model, Quarterly Journal of the Royal Meteorological Society 131 (2005) 2431–2454.

[16] F.X. Giraldo, T. Warburton, A nodal triangle-based spectral element method for the shallow water equations on the sphere, Journal of Computational Physics 207 (2005) 129–150.

[17] J.S. Hesthaven, From electrostatics to almost optimal nodal sets for polynomial interpolation in a simplex, SIAM Journal on Numerical Analysis 35 (1998) 655–676.

[18] C.Q. Hu, C.W. Shu, Weighted essentially non-oscillatory schemes on triangular meshes, Journal of Computational Physics 150 (1999) 97–127.

[19] W. Hundsdorer, J. Jaffré, Implicit-explicit time stepping with spatial discontinuous finite elements, Applied Numerical Mathematics 45 (2003) 231–254.

[20] G.E. Karniadakis, M. Israeli, S.A. Orszag, High-order splitting methods for the incompressible Navier–Stokes equations, Journal of Computational Physics 97 (1991) 414–443.

[21] T. Koornwinder, Two-variable analogues of the classical orthogonal polynomials, in: R.A. Askey (Ed.), Theory and Applications of Special Functions, Academic Press, San Diego, 1975.

[22] J. Lyness, R. Cools, A survey of numerical cubature over triangles, Applied Mathematics 48 (1994) 127–150.

[23] J. Proriol, Sur une famille de polynomes á deux variables orthogonaux dans un triangle, C.R. Acadamic Science Paris 257 (1957) 2459.

[24] J.A. Rossmanith, D.S. Bale, R.J. LeVeque, A wave propagation algorithm for hyperbolic systems on curved manifolds, Journal of Computational Physics 199 (2004) 631–662.

[25] J. Sanchez, M. Net, B. García-Archilla, C. Simó, Newton–Krylov continuation of periodic orbits for Navier–Stokes flows, Journal of Computational Physics 201 (2004) 13–33.

[26] C.W. Shu, High-order finite difference and finite volume WENO schemes and discontinuous Galerkin methods for CFD, International Journal of Computational Fluid Dynamics 17 (2003) 107–118.

[27] A.H. Stroud, Approximate Calculation of Multiple Integrals, Prentice-Hall Publishing, New Jersey, 1971.

[28] M.A. Taylor, B.A. Wingate, R.E. Vincent, An algorithm for computing Fekete points in the triangle, SIAM Journal on Numerical Analysis 38 (2000) 1707–1720.

[29] E.F. Toro, Riemann Solvers and Numerical Methods for Fluid Dynamics, A Practical Introduction, Springer, New York, 1999.

[30] Z.J. Wang, L. Zhang, Y. Liu, Spectral (finite) volume method for conservation laws on unstructured grids IV: extension to two-dimensional systems, Journal of Computational Physics 194 (2004) 716–741.

[31] D.L. Williamson, J.B. Drake, J.J. Hack, R. Jakob, P.N. Swarztrauber, A standard test set for numerical approximations to the shallow water equations in spherical geometry, Journal of Computational Physics 102 (1992) 211–224.